Received: 13 October 2021 | Revised: 5 November 2021 | Accepted: 5 November 2021

DOI: 10.1002/pol.20210766

RESEARCH ARTICLE

JOURNAL OF POLYMER SCIENCE WILEY

Cryo-spun encapsulation of polyaniline-based conducting hydrogels with high sensitivity, wide-range linearity, and environmental stability for fibrous strain sensors

Qichun Feng[1] | **Kening Wan**[3] | **Chao Zhang**[1] | **Tianxi Liu**[1,2]

[1]State Key Laboratory for Modification of Chemical Fibers and Polymer Materials, The Key Laboratory of High-Performance Fiber and Product, Ministry of Education, College of Materials Science and Engineering, Donghua University, Shanghai, P.R. China

[2]Key Laboratory of Synthetic and Biological Colloids, Ministry of Education, School of Chemical and Material Engineering, Jiangnan University, Wuxi, P.R. China

[3]School of Engineering and Materials Science, Queen Mary University of London, London, UK

Correspondence
Chao Zhang and Tianxi Liu, State Key Laboratory for Modification of Chemical Fibers and Polymer Materials, The Key Laboratory of High-Performance Fiber and Product, Ministry of Education, College of Materials Science and Engineering, Donghua University, Shanghai 201620, China.
Email: czhang@dhu.edu.cn and txliu@fudan.edu.cn

Funding information
Fundamental Research Funds for the Central Universities, Grant/Award Number: 2232020G-02; National Natural Science Foundation of China, Grant/Award Numbers: 21875033, 52122303

Abstract

Wearable strain sensors are widely engaged in the fields of soft robotics, health monitoring, and human-machine interfaces. However, low sensitivity, poor environmental resistance, and low-air permeability of wearable strain sensors severely limit their practical applications. Herein, a coaxial fiber consisting of a polyvinyl alcohol/polyaniline hydrogel (PPH) core and a thermoplastic elastomer (styrene-isoprene-styrene block copolymer, SIS) sheath was fabricated by a cryo-spun encapsulation strategy. The as-obtained PPH@SIS fiber exhibited high stretchability (>200% strain), large conductivity (0.51 $mS.cm^{-1}$) and high-yet-linear sensitivity (gauge factor of 2.4) when being directly used as a fibrous strain sensor. The resultant PPH@SIS fibrous strain sensor showed a stable response at a broad temperature range from −50 to 50°C to various strains (0% ∼ 100%) and frequencies (0 ∼ 2 Hz). As a demonstration, the PPH@SIS fibrous strain sensors are capable of identifying fast and slow bendings of dummy joints, showing excellent wearability, high sensitivity, and wide detecting range. This work therefore provides a unique cryo-spun encapsulation strategy for fabricating coaxial conductive fibers promising for wearable sensors with high sensitivity, excellent wearing comfort, and resistance to extreme environments.

KEYWORDS

coaxial fibers, conducting polymer hydrogels, cryo-spun encapsulation, environmental stability, wearable strain sensors

1 | INTRODUCTION

Rapid developments of electronics and information technologies have prompted an increasing demand for wearable and stretchable electronic devices.[1] Currently, stretchable strain sensors based on a structural design of silicon, metal, and ceramic materials are widely used in biomedicine, automotive, and other fields.[2] However, shortcomings of high density, low sensitivity, and narrow strain range made them unsuitable to meet the requirements for extremely cold and vacuum environments.[3] Besides, air permeability is also necessary for wearable sensors in consider of wearable comfort.[2d,f,4] Therefore, the fabrication of light-weighted, resistant to extreme

environments, highly sensitive and stretchable conductive fibers are great potential candidates for next-generation wearable fibrous structure and weaving strain sensors.

Ionic conductors like ionic liquids, ionic gels, and hydrogels have the characteristics of low modulus, which have been used for fabricating fibrous stretchable ionic conductors.[5] As a new type of strain sensing material, stretchable fibrous ionic conductors have been applied to fabricating wearable strain sensors and optical sensors.[6] However, ions in the conductors as carriers are uniformly distributed in the entire material, leading to a negligible change of conductive paths under deformations.[7] As a result, fibrous ionic conductors usually show low sensitivity to accurately identifying small deformation of human motions. Besides, fibrous ionic conductors are normally hard to achieve long-term and wide-range responses especially to withstand extreme environmental conditions.[7c,8] These drawbacks greatly limited the practical applications of fibrous ionic conductors in wearable fibrous and weaving strain sensors. The development of new-type and high-performance fibrous stretchable ionic conductors has prospects while meeting great challenges.

Herein, a cryo-spun encapsulation strategy was proposed to continuously fabricate a polyvinyl alcohol/polyaniline hydrogel@thermoplastic elastomer (styrene-isoprene-styrene block copolymer as the thermoplastic elastomer, SIS) (PPH@SIS) coaxial fiber. The cryo-spun encapsulation strategy consists of two steps. First, a coaxial wet-spun with PPH precursor solution and SIS solution as the core and sheath spinning solution, respectively, was used for the formation of a coaxial fiber with PPH precursor core and SIS sheath. Second, the fresh-made coaxial fiber was frozen to further form the PPH core via subsequent cryopolymerziation. The aniline monomers among the PPH precursor were capable of in situ polymerizing into PANI nanostructures within PVA skeletons under frozen states. An electric and ionic dual conductive network was achieved among the PPH, greatly improving the sensitivity of PPH@SIS fibrous strain sensors. The mixed solvent of water and ethylene glycol (EG) reduced the freezing point of the resultant PPH, thereby significantly enhancing the low-temperature resistance of coaxial fibers. The high stretchability of the SIS sheath endowed the PPH@SIS fibers with a wide reversible strain range and high-fatigue resistance. In addition, the high hydrophobicity of the SIS sheath protected the PPH core from any evaporation, endowing the PPH@SIS fibers with long-term working life. As a proof of concept, the PPH@SIS fiber was attached to dummy joints as a wearable strain sensor, capable of monitoring the joint movements in real-time with high sensitivity and extremely low hysteresis. The cryo-spun encapsulation strategy provides a new avenue for the development of fibrous strain sensing materials with high stretchability, extreme-temperature resistance, large, and linear sensitivity.

2 | RESULTS AND DISCUSSION

Herein, a cryo-spun encapsulation strategy was proposed for obtaining a coaxial fiber (PPH@SIS) with fibrous core and sheath of PPH and SIS (Figure 1A), respectively. Ethanol is unable to dissolve SIS, while ethanol and dichloromethane (CH_2Cl_2) are mutually soluble. When the sheath solution of SIS/CH_2Cl_2 was squeezed into the ethanol coagulation bath from the outer channel of the coaxial needle, the CH_2Cl_2 was quickly extracted by the ethanol, and thereby a hollow SIS fiber tube was produced. Afterward, the core solution of PPH precursor (pre-PPH) was then injected into the hollow SIS fiber tube from the inner channel of the coaxial needle for the formation of pre-PPH@SIS fibers. The cryo-spun encapsulation strategy for the preparation of pre-PPH@SIS fibers was simple yet efficient for continuous spinning (Movie S1). The PPH@SIS fibers were finally obtained by further sequentially treating the pre-PPH@SIS fibers at -100 and $-20^{\circ}C$, respectively, for cryopolymerizing the aniline monomers into PANI nanostructures among the PPH core. PVA skeletons with physically crosslinking sites were also formed inside the PPH core at low temperatures.

The cryo-spun encapsulation strategy can fabricate continuous PPH@SIS fibers with a length of more than 6 meters. The PPH@SIS fibers were collected on a winding shaft (Figure 1B) and subsequent ethanol-washing (Figure 1C), indicating that the cryo-spun encapsulation strategy is capable of preparing the PPH@SIS coaxial fibers on a large scale. The PPH@SIS fiber was capable of being stretched for >200% strain (Figure S1) and bearing a 200 g weights (Figure 1D), indicating that the PPH@SIS fibers showed high stretchability and mechanical stability. The surface of PPH@SIS fiber was smooth (Figure 1E), and the boundary between the core and sheath of PPH@SIS fibers was distinct, indicating the core-sheath structure of PPH@SIS fibers were chemically stable (Figure 1F), in which the core diameter was ~900 μm and the thickness of the sheath was ~90 μm. Field emission scanning electron microscopy (FESEM) image of the PPH core of PPH@SIS fibers indicated that the PANI nanostructures were evenly and uniformly distributed within the PVA skeleton (Figure 1G).

Structural characterizations of PPH are shown in Figure 2. Similar to the fabrication of PPH@SIS fibers, the solution containing aniline monomers and PVA was

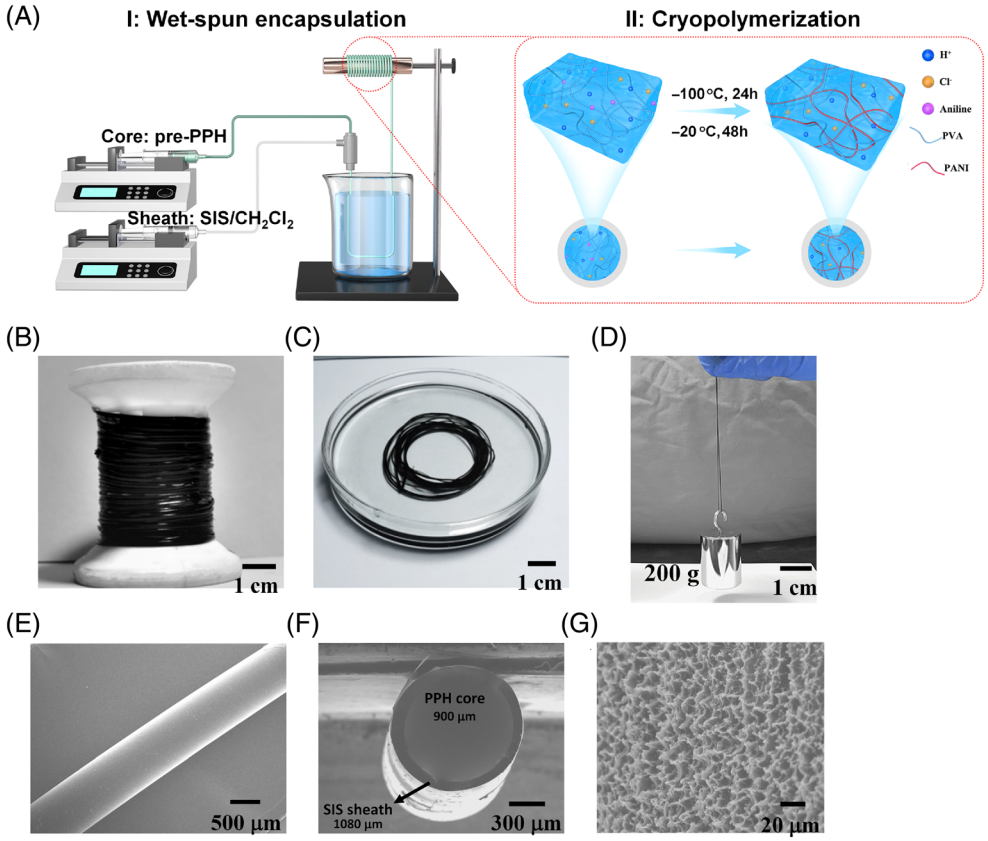

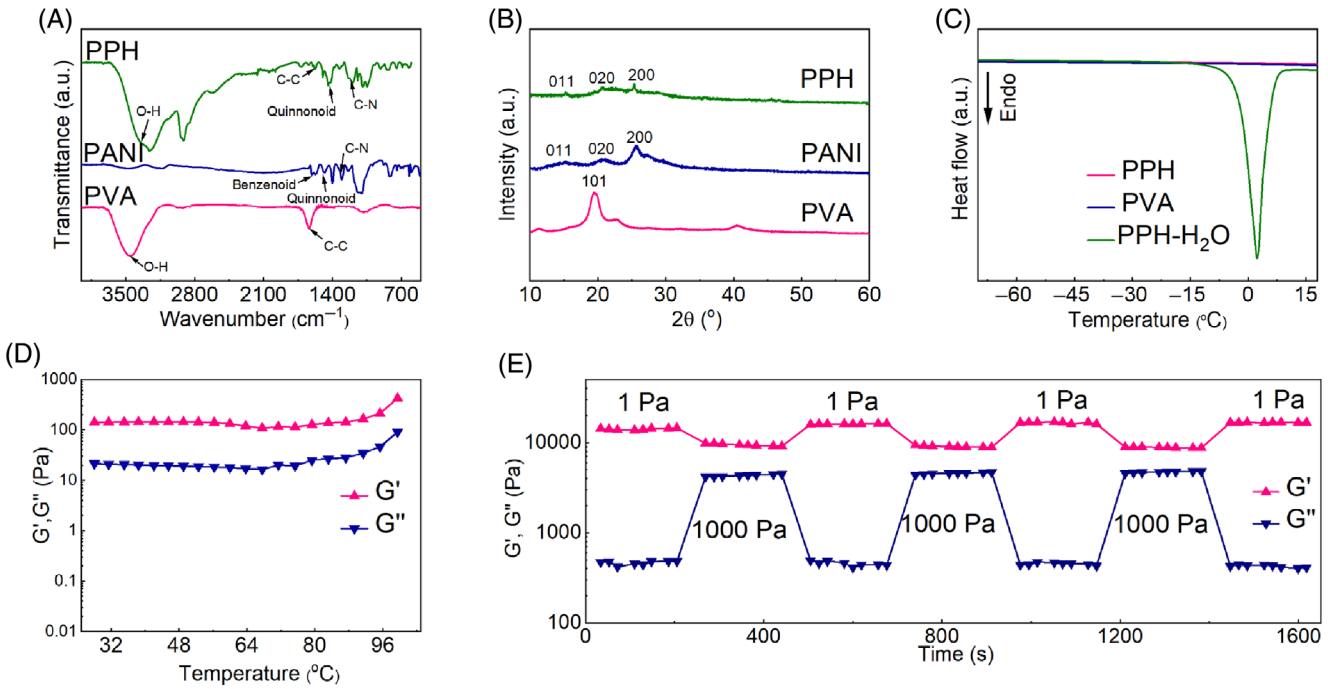

FIGURE 1 (A) Schematic of the fabrication of the PPH@SIS fiber via a cryo-spun encapsulation strategy. Photographs showing the as-obtained PPH@SIS fiber (B) collected on a spindle and (C) immersed in an ethanol bath. (D) Photograph showing the as-obtained PPH@SIS fiber holding a 200 g weight. (E) Surface and (F) cross-section SEM images of the PPH@SIS fiber. (G) SEM image of the freeze-dried PPH core among the PPH@SIS fiber. PPH, polyaniline hydrogel; SEM, scanning electron microscopy; SIS, styrene-isoprene-styrene

FIGURE 2 (A) FT-IR spectra and (B) XRD patterns of PPH, PANI, and PVA. (C) DSC curves of PPH, PVA, and PPH-H_2O. (D) Temperature dependence of G′ and G″ of PPH. (E) Continuous step-stress measurements of PPH at 1 and 1000 pa, respectively. DSC, differential scanning calorimeter; FT-IR, Fourier transform infrared spectra; PPH, polyaniline hydrogel; SIS, styrene-isoprene-styrene; XRD, x-ray diffraction

first placed at −100°C for 24 h while PVA skeletons were also formed. Free ions, derived from APS and HCl, were evenly distributed within the PPH, and an ionic conductive network was formed during the freezing process. The reaction system was then transferred from −100 to −20°C and maintained for another 48 h. The aniline monomers were in situ cryopolymerized into PANI nanostructures and uniformly distributed in PVA skeletons. The electrical conductive network was constituted from the in situ formed PANI nanostructures.

The PPH was able to retain at the bottle bottom after cryopolymerization (Figure S2), indicating that the gel network of PPH was formed. To investigate the influence of aniline monomers and EG on the gel networks in PPH, the PVA organogel without the addition of aniline monomers and the PPH-H_2O without the addition of EG were also synthesized, respectively. Strain sweep measurements of PVA organogel, PPH-H_2O and PPH were conducted for understanding the structural stability of the gel networks.[9] The values of storage modulus (G′) for these three gels were all much higher than those of loss modulus (G″) in the linear range of 1%–1000% (Figure S3a) and wide angular frequency range of 1–100 rad s^{-1} (Figure S3b). These elastic characteristics of PVA organogel, PPH-H_2O and PPH were consistent with the performance of hydrogels reported in the literature, confirming that the gel networks were successfully constructed by PVA organogels in the PPH-H_2O and PPH.[9a,10] It is worth noting that the addition of EG did not change the values of G′ and G″, indicating that the EG would not damage the gel network of PVA. Fourier transform infrared spectra (FT-IR) of PANI, PVA organogel and PPH were characterized and shown in Figure 2A. The peaks of 3458 and 1635 cm^{-1} in PVA belonged to O—H and C—C, respectively.[11] The O—H successfully formed hydrogen bonds with N-containing functional groups in the PANI (O—H···N—C), which caused the O—H in PVA to shift to 3264 cm^{-1} in the PPH. However, the peak at 1635 cm^{-1} attributed to the C—C bond of PVA in the PPH did not shift, suggesting that the C—C in PVA did not directly form bonds with the PANI. The peak of 1317 cm^{-1} belonged to the C—N of PANI, but the C—N in the PPH shifted to 1186 cm^{-1}, attributing to the formation of hydrogen bonding between the C—N and O—H in PVA. Similarly, since the quinone in PANI (1448 cm^{-1}) and the O—H in PVA could form hydrogen bonds, the quinone in PPH shifted to 1436 cm^{-1}. Raman spectra of PANI showed peaks of 1130, 1188, 1347, and 1543 cm^{-1} (Figure S4), belonging to C—H bending, C—N stretching (quinoid ring), C—N^+ stretching (semiquinoid ring), and C—C deformation (semiquinoid ring), respectively. The Raman results indicated that the proton-doped PANI networks were successfully synthesized.[12] The x-ray diffraction (XRD) patterns showed the peaks in PPH were superimposed by PANI and PVA and shifted slightly (Figure 2B), indicating that PANI was successfully introduced into the PVA networks. Differential scanning calorimeter (DSC) measurements were used to evaluate the effect of EG and aniline monomers on the anti-freezing performance of PPH (Figure 2C). A sharp peak at ∼2.3°C was observed on the DSC curve of PPH-H_2O, showing that the PPH was frozen below 0°C without the addition of EG. Since the PVA skeletons in PPH-H_2O were established during the freeze–thaw process, the freezing point of PPH-H_2O was slightly higher than that of water. However, no peaks of PPH and PVA organogel were observed from 15 to −70°C, indicating that the H_2O-EG mixed solvent significantly increased the freezing point of PPH and aniline monomers would not damage the anti-freezing performance of PPH. The PPH had excellent low-temperature resistance, which was of great significance to using the as-obtained electronic devices in a low-temperature environment. The changes of G′ and G″ values under variable temperatures accurately reflected the stability of gel networks under different temperatures.[9a,b,10b] Looking at the PPH (Figure 2D), the G′ value was remained greater than that of G″ in the range of 25 ∼ 90°C, indicating that the gel network of PPH was stable at the range of 25 ∼ 90°C. In the range of 90 ∼ 100°C, the difference between G′ and G″ began to decrease, showing that the gel network of PPH was partially destroyed in this temperature range. Therefore, the PPH had the potentials to work stably under 90°C. The varying intensities of stress were used to simulate the changes of PPH under external force and standing (Figure 2E). The values of G′ and G″ for PPH were constant under small applied stress of 1 Pa (G′ > G″), indicating the elastic property of PPH was stable without external force. When the applied stress moved to 1000 Pa, the values of G′ and G″ decreased rapidly and remained almost unchanged, respectively, and the values of G′ kept greater than that of G″. This was because the gel network of PPH was partially destroyed by the applied stress. When the stress was back to 1 Pa, the values of G′ and G″ immediately return to the original state, suggesting that the gel network of PPH was self-healed in a static environment. After 30 min (3 cycles) of alternately applied stress (1 and 1000 Pa), the values of G′ and G″ of PPH were still able to return to their original state. This result showed that the gel network of PPH had excellent self-healing ability.

To investigate the influences of PVA and PANI nanostructures on the mechanical properties of the PPH@SIS, the hollow SIS and PVA@SIS were synthesized, respectively. The hollow SIS, PVA@SIS, and PPH@SIS fibers were stretched for 5000 cycles at a 100%

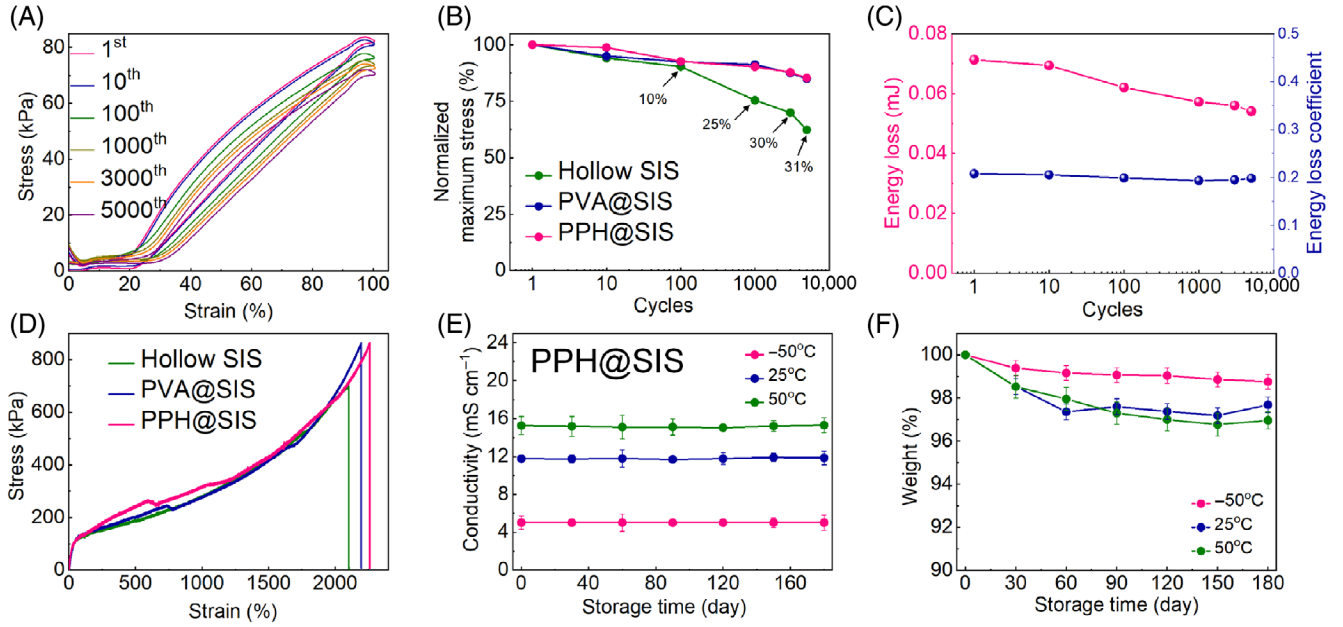

FIGURE 3 (A) Cyclic loading/unloading tests of the PPH@SIS fiber. (B) Normalized maximum stress of the hollow SIS, PVA@SIS, and PPH@SIS fibers, respectively. (C) Cycle-dependent energy loss and energy loss coefficient of the PPH@SIS fiber. (D) Typical strain–stress curves of the hollow SIS, PVA@SIS, and PPH@SIS fibers. (E) Conductivity and (F) weight changes of the PPH@SIS fiber at various temperatures. PPH, polyaniline hydrogel; SIS, styrene-isoprene-styrene

strain, and the results of plastic deformations based on the tensile experiments are shown in Figure 3A, Figures S5 and S6.[13] The plastic deformations of hollow SIS, PVA@SIS, and PPH@SIS fibers were 30%, 28%, and 27%, respectively. The decreases in plastic deformation were attributed to the stable coaxial structure. The maximum stress of the three fibers at different cycles was normalized, and the values of hollow SIS fiber had been directly marked in Figure 3B. The maximum stress of hollow SIS fiber decreased by 10% at the 100^{th} cycle, and then cliff-like faded to 25% (1000^{th} cycle), 30% (3000^{th} cycle), and finally stabilized at 31% (5000^{th} cycle). The introduction of PVA into SIS fibers effectively prevented its maximum stress from the sharp decrease after 1000 cycles. The maximum stress of PVA@SIS only had 9% (1000^{th} cycle), 13% (3000^{th} cycle), and 15% (5000^{th} cycle) reductions after the cyclic stretching-releasing processes. This was because PVA effectively reduced the stress concentrations of the SIS sheath during the stretching of PPH@SIS fiber. Therefore, the PVA@SIS fiber exhibited a higher fatigue resistance than that of hollow SIS fiber. The maximum stress decrease of PPH@SIS fibers was similar to that of PVA@SIS fibers, indicating that the PANI nanostructures would not destroy the mechanical performance of PPH@SIS fibers. Figure S7 is the loading-unloading curve of PPH@SIS fibers at different frequencies. Under a 100% strain, each time-stress curves of PPH@SIS fibers were almost symmetrical, which further showed the excellent mechanical performance of PPH@SIS fibers. The tensile work and energy loss as a function of time for the PPH@SIS fiber were calculated (Figure S8). Taking the first cycle as an example, the tensile work during loading (U) was 0.34 mJ. When the unloading was complete, the work, which was energy dissipation (ΔU), remained at 0.07 mJ. The energy loss coefficient (η) can be calculated from Equation (1):

$$\eta = \frac{\Delta U}{U}. \tag{1}$$

At this time, η was 0.21, and ΔU was 0.071 mJ. The ΔU decreased continuously within 100 cycles and stabilizes (0.071 ~ 0.062 mJ) (Figure 3C). The reason for the high ΔU within 100 cycles was that the PPH@SIS fibers suffered from extensive and inevitable structural damages during the loading/unloading process. After 100 cycles of loading and unloading, an almost stable η was obtained (0.0193 ~ 0.198), and ΔU was also stabilized at 0.057 ~ 0.054 mJ. The elongation at break and fracture mechanical strength of hollow SIS fibers was lower than that of PVA@SIS and PPH@SIS fibers (Figure 3D). To observe the mechanical properties of hollow SIS fiber, PVA@SIS fiber and PPH@SIS fiber more clearly, the results were summarized and shown in Figure S9. The elongation at break of hollow SIS fibers was ~2200%,

which was slightly lower than that of PVA@SIS fiber (~2300%) and PPH@SIS (~2370%). These results were attributed to the PVA and PPH were all capable of providing stress dispersion for the SIS sheath, which were beneficial to increase the maximum strain of SIS. Similarly, the fracture strength of hollow SIS fiber (1480 kPa) was lower than that of PVA@SIS fiber (1810 kPa) and PPH@SIS (1820 kPa), and the results were also attributed to the energy distribution of PVA and PPH for the SIS. The tensile fracture strength and elongation at break of PPH@SIS fibers were both slightly higher than that of PVA@SIS fibers. The above results showed that the PPH@SIS fiber had excellent mechanical properties. Figure 3E presented the relationships between the conductivity of PPH@SIS fibers under various temperatures and storage time. With the change of temperature from −50 to 50°C, the conductivity of PPH@SIS fibers increased from 0.33 to 0.51 mS cm^{-1}. It was following the theory of ionic conductivity that the rates of ion migration in the PPH network were limited by the low temperature. The lowest conductivity of the PVA@SIS fibers was obtained under the low temperature at −50°C (-Figure S10). This was because the core PVA in PVA@SIS fiber had become solid-state, and ions were hard movable directionally.[14] Under a constant temperature, the conductivity of PPH@SIS did not vary with storage time. The results were attributed to the extremely low-vapor pressure of PPH given by the mixed solvents of EG-H_2O. In addition, the SIS sheath had excellent hydrophobicity and can inhibit internal water vaporation. Therefore, the PPH@SIS fibers were able to maintain a stable weight and conductivity at different temperatures (Figure 3F).

Figure 4A was the working curve of the PPH@SIS fibrous strain sensor at 0% ~ 100% dynamic tensile strain. Stable and repeatable working curves were observed under the same strains, and the step-like shapes of the working curve were presented under different strains, which was consistent with the applied strain signals. This result indicated that PPH@SIS fiber could work stably under wide and complex deformations. Similarly, the PPH@SIS fibers also exhibited the resistance-strain response that was resistant to complex frequencies (Figure 4B). The working curves of PPH@SIS fibers were gradually dense with the working frequencies increased. This strain-resistant and frequency-resistant performance was beneficial for PPH@SIS fibers to adapt to monitoring complex human movements, such as variable speed running. Figure S11 showed the hysteresis performance of PPH@SIS fibers. The small area enclosed by the tensile working curve and the release working curve of PPH@SIS fibers indicated their low hysteresis. Figure 4C showed that the response time of PPH@SIS fiber was less than 120 ms. The low hysteresis and fast response performances of PPH@SIS were attributed to the dual

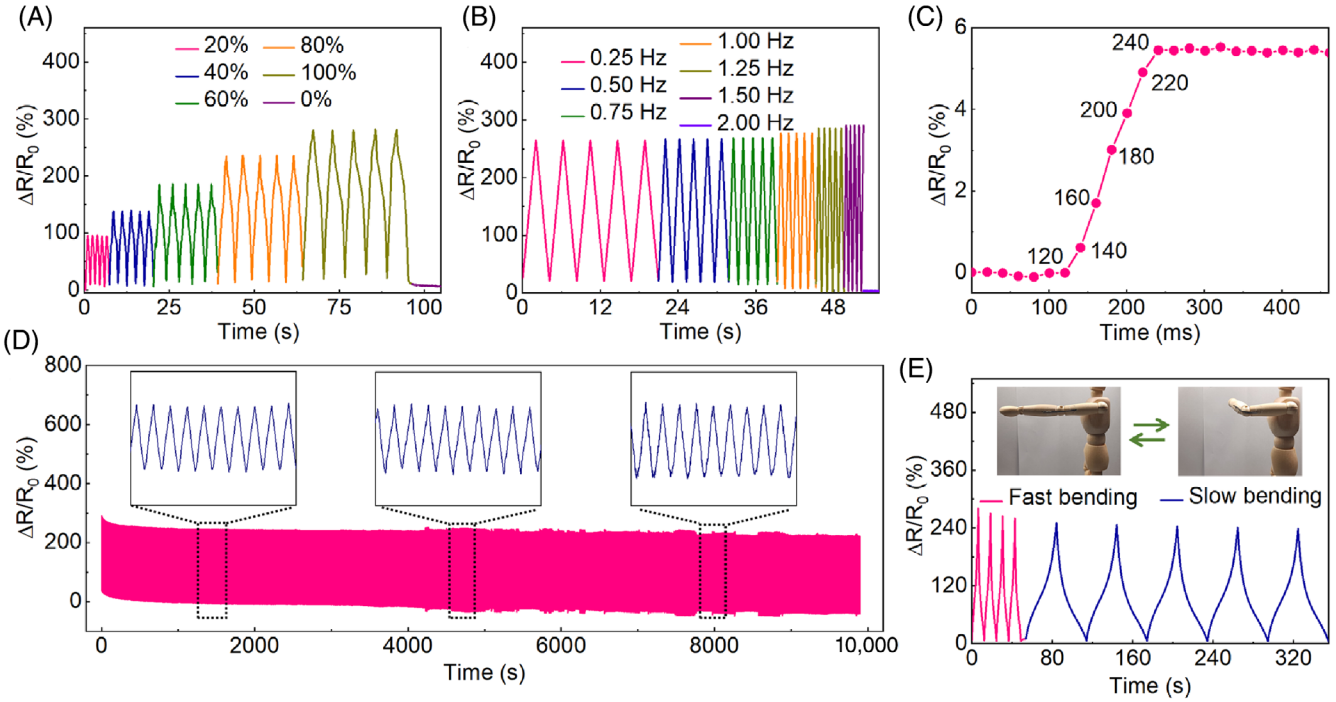

FIGURE 4 Relative resistance variations of the PPH@SIS fiber at (A) various tensile strains and (B) frequencies, respectively. (C) Response time and (D) cycling stability of the PPH@SIS fiber. (E) Relative resistance variations of the PPH@SIS fiber monitoring elbow bending. PPH, polyaniline hydrogel; SIS, styrene-isoprene-styrene

conductive network of PPH and the excellent mechanical property of PPH@SIS fibers. More than that, these strain performances also laid solid foundations for PPH@SIS fibers as an instant response sensing material. Figure 4D exhibited the durability of PPH@SIS fibers. PPH@SIS fibers were capable of running stably for 10,000 s (3000 cycles) under a 100% strain. The working curves of PPH@SIS fiber in the beginning (0 ~ 300 s) had a slight drop. This was due to unavoidable microstructure damages of PPH@SIS fibers. The insets in Figure 4D were the working curves of PPH@SIS fibers at different stages (initial, intermediate, and final stages). The great repeated working curves at different stages verified the PPH@SIS fibers had excellent cycle stability. For proof-of-concept, PPH@SIS fibers had been worn on a dummy (insets in Figure 4E, Figures S12 and S13) for characterizing the wearable performance of PPH@SIS fibers. During the process of wearing on and taking off the PPH@SIS fibers, no residuals were found on the dummy limbs, indicating that PPH@SIS fibers were suitable for wearing. Figure 4E was the working curve of PPH@SIS fibers monitoring the movements of dummy elbow. When the dummy was moving, the working curves of PPH@SIS fibers showed symmetry in real-time, which meant that PPH@SIS fibers could accurately recognize dummy movements and identify slow and fast movements. Similarly, the PPH@SIS fibers could also accurately identify the bending movements of the dummy finger, including the slow bending, rest and fast bending (Figure S12). Marching, resting and leg lifting were also identified by the PPH@SIS fibrous sensors (Figure S13). This ability to accurately identify different joint motions showed that PPH@SIS fibers could be used as multirole wearable sensing materials. The fibrous strain sensors based on PPH@SIS were also worn on the human body, and the marching movements were monitored in real-time (Movie S2).

The working performance of the PPH@SIS fibers in extremely low-temperature environments was also investigated. Figure 5A and Figure S14 were the resistance change mechanism of PPH@SIS and PVA@SIS fibers when being stretched, respectively. Figure 5A showed the PNAI nanostructures were broken into short unconnected nanostructures during the stretching. However, Figure S14 showed the concentration of ions only changed uniformly during the stretching of PVA. The concentration of ions, derived from APS and HCl, would uniformly decrease with the deformation of the PVA during the PVA@SIS fibers being stretched (Figure S14).

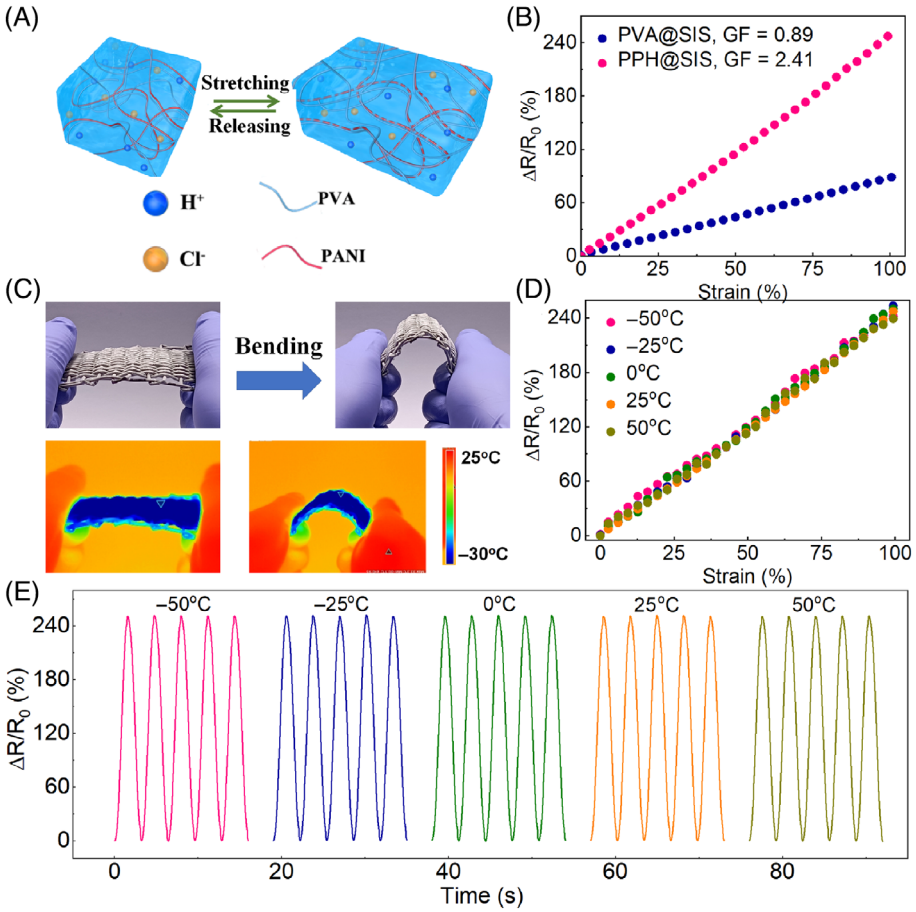

FIGURE 5 (A) Schematic of the evolution of conductive paths of PANI-based electric conductive network and ion-based ionic conductive network of the PPH@SIS fiber during the stretching and releasing process. (B) GF values of the PPH@SIS and PVA@SIS fibers, respectively. (C) Photographs showing the bending of a woven fabric of PPH@SIS fibers at −30°C. (D) GF values and (E) relative resistance variations of the PPH@SIS fiber at various temperatures. PPH, polyaniline hydrogel; SIS, styrene-isoprene-styrene

Since ions were carriers in PVA@SIS fibers, the uniform changes of ion concentration would lead the PVA@SIS fibers to lack drastic changes in the conductive paths during the stretching process, which in turn made the resistance change of PVA@SIS fibers small. On the contrary, although the ion concentrations in PPH@SIS fiber still changed uniformly with the deformation of PPH, the PANI nanostructures in PPH would break during the deformation process of PPH, which made the PPH@SIS fiber have a high-resistance change (Figure 5A). The calculation of gauge factors (GF) was as follows:

$$GF = \frac{\Delta R}{\Delta \varepsilon}. \quad (2)$$

Here, ΔR was the value of resistance change and $\Delta \varepsilon$ was the value of strain change. Therefore, the GF values depended on the values of resistance change when the strain was the same. The GF values of the PPH@SIS fibers were higher than the PVA@SIS fibers in theory. Figure 5B showed the GF values of actual measurements for the PPH@SIS fibers at different temperatures, which was $\sim$2.4 ($R^2 = 0.99$). However, the GF value of PVA@SIS fibers at room temperature was only 0.89 ($R^2 = 0.99$). Figure 5C showed that PPH@SIS-based woven fabrics could be bent at $-30^{\circ}C$, which preliminarily showed that PPH@SIS fiber could work at low temperatures. Figure 5D is the working curves of PPH@SIS fiber at different temperatures. At each temperature, the working curves of PPH@SIS fiber were symmetrical and similar, indicating that PPH@SIS fiber had stable sensing performance at different temperatures (Figure 5E). These results showed PPH@SIS fiber had the potentials to work in a variable temperature environment.

3 | CONCLUSION

In summary, the PPH with an electric and ionic dual conductive network was designed and prepared. The as-obtained PPH was encapsulated in an SIS sheath by a cryo-spun encapsulation strategy for realizing continuous preparation of a PPH@SIS fiber. The dual conductive networks endowed the PPH@SIS fibers with an excellent conductivity (0.51 mS cm^{-1}) and high-GF value (2.4). Anti-freezing solvent (EG-H_2O mixture) and the hydrophobic SIS sheath together ensured the stability of the weight and conductivity of PPH@SIS fibers for 6 months at various temperatures. The excellent anti-freezing performance and the stability endowed the PPH@SIS fibers with similar and repeatable working curves at extreme and room temperatures. Besides, the PPH@SIS fibers were also able to work stably under various frequencies (0 $\sim$ 2 Hz) and deformations (0% $\sim$ 100% strain) for more than 3000 cycles. In addition, the wearable performance of PPH@SIS fibers had also been conceptually verified. It was directly attached to the dummy arm, finger, and knee, and could monitor all subtle changes in the different amplitudes and rhythms. The cryo-spun encapsulation strategy thus opens a new avenue to fabricate wearable strain sensing fibers with high sensitivity, wide-range linearity range, and environmental stability.

4 | EXPERIMENTAL SECTION

4.1 | Materials

Aniline (≥99.5%), PVA (M_w: 85000 $\sim$ 124,000, 99 + % hydrolyzed), styrene-isoprene-styrene block copolymer (SIS, styrene 22 wt%), ethanol (≥99.5%), and dichloromethane (CH_2Cl_2, ≥99.5%) were purchased from Sigma-Aldrich. Hydrochloric acid (HCl, CP, 36% $\sim$ 38%) and ammonium persulfate (APS, ≥98.0%) were purchased from Sinopharm Chemicals. Deionized (DI) water was used throughout the experiments. All the chemicals were used as received unless otherwise stated.

4.2 | Preparations of PPH@SIS, PVA@SIS, and hollow SIS fibers

SIS spinning solution for fabricating the fiber sheath was prepared as follows: 10 g of SIS and 20 g of CH_2Cl_2 were mixed and stirred at room temperature until dissolved. PPH spinning solution for fabricating the fiber core of PPH@SIS was prepared as follows: 0.83 mL of HCl, 0.23 g of APS, 0.1 mL of aniline and 4.5 g of EG were added into 10 mL of PVA solution (18 wt%). PVA spinning solution for fabricating the fiber core of PVA@SIS was prepared as follows: 0.83 mL of HCl, 0.23 g of APS and 4.5 g of EG were added into 10 mL of PVA solution (18 wt%). PPH-H_2O was synthesized as follows: 0.83 mL of HCl, 0.23 g of APS and 0.1 mL of aniline were added into 10 mL of PVA solution (10 wt%). All the spinning solution was degassed for 10 min before wet spinning. A coaxial needle consisted of a 21G needle (inner channel) and a 15G needle (outer channel) was used for cryo-spun encapsulation fabrication of PPH@SIS fibers.[15] First, the SIS spinning solution was extruded from the outer channel into an ethanol coagulation bath at a speed of 400 μL min^{-1}. The CH_2Cl_2 among the spinning solution was quickly exchanged with ethanol for the formation of SIS fiber sheath. Subsequently, the spinning solution of

PPH precursors was extruded from the inner channel at a speed of 200 μL min^{-1}. The as-spun continuous fiber was transferred to −100°C and maintained for 24 h, and then the temperature was raised to −20°C and maintained for another 48 h. Finally, the PPH@SIS fiber was obtained after being washed with ethanol and air-dried at room temperature. Cryo-spun encapsulation fabrications of PVA@SIS fibers were similar to that of PPH@SIS fibers except for the use of PVA spinning solution, instead of PPH precursors. SIS hollow fiber was obtained by extracting the PPH core from the as-spun PPH@SIS fibers.

4.3 | Characterizations

Freeze-dried samples (PANI, PPH, and PVA) were analyzed by Fourier transform infrared spectroscopy (FT-IR, Nicolet iS10, Thermo Fisher Scientific), XRD patterns (Cu K_α, Bruker D8) and Raman spectra (λ_{exc} = 631 nm, InVia Reflex). Differential scanning calorimetry (DSC, Q250, TA Instruments) was carried out in a nitrogen atmosphere. Rheological measurements were investigated by using a 25 mm parallel-plate geometry (MARS60-iS10, HAAKE). Morphologies of fiber samples were measured by field-emission scanning electron microscopy (SEM, JSM-IT300). Mechanical tests were performed on a universal testing machine (SANS UTM2102) equipped with a 100 N sensor. Thermographic images were taken by an infrared thermal camera (TiS40, Fluke).

4.4 | Measurements of fibrous strain sensors based on PPH@SIS and PVA@SIS fibers

SIS sheath has two different glassy transition temperatures (−60 and 70°C), assigned to isoprene and styrene segments, respectively. A viscous flowing state of the SIS sheath was formed when the temperature exceeded 70°C. In this study, two ends of the PPH@SIS fiber were sealed by a hot-pressing method. Copper wires were inserted into the two ends of a PPH@SIS fiber, and hot-pressing was used to seal the two ends of the PPH@SIS fiber. The detailed conditions of hot-pressing were set at 100°C and 1 MPa for 30 s. Similarly, PVA@SIS fiber was also sealed by the same hot-pressing method. The as-obtained fibrous strain sensors were placed in a motorized actuating system, consisting of a tensile testing machine (UTM2000, SANS) and a source meter (2612B, Keithley). To monitor the movements of dummy joints, the fibrous strain sensors were attached to dummy joints and connected with the source meter through copper wires.

ACKNOWLEDGMENTS

The authors acknowledge the funding supports from the Fundamental Research Funds for the Central Universities (2232020G-02), the National Natural Science Foundation of China (52122303, 21875033).

DATA AVAILABILITY STATEMENT

All data during the study are available from the corresponding author by request.

ORCID

Chao Zhang https://orcid.org/0000-0003-1255-7183

REFERENCES

[1] (a) W. Ma, Y. Zhang, S. Pan, Y. Cheng, Z. Shao, H. Xiang, G. Chen, L. Zhu, W. Weng, H. Bai, M. Zhu, *Chem. Soc. Rev.* **2021**, *50*, 7009. (b) W. Hu, L. Wan, Y. Jian, C. Ren, K. Jin, X. Su, X. Bai, H. Haick, M. Yao, W. Wu, *Adv. Mater. Technol.* **2019**, *4*, 1800488. (c) S. Yuvaraja, A. Nawaz, Q. Liu, D. Dubal, S. G. Surya, K. N. Salama, P. Sonar, *Chem. Soc. Rev.* **2020**, *49*, 3423. (d) J. Shi, S. Liu, L. Zhang, B. Yang, L. Shu, Y. Yang, M. Ren, Y. Wang, J. Chen, W. Chen, Y. Chai, X. Tao, *Adv. Mater.* **2020**, *32*, 1901958. (e) H. R. Lim, H. S. Kim, R. Qazi, Y. T. Kwon, J. W. Jeong, W. H. Yeo, *Adv. Mater.* **2020**, *32*, 1901924. (f) L. Wang, D. Chen, K. Jiang, G. Shen, *Chem. Soc. Rev.* **2017**, *46*, 6764. (g) D. C. Kim, H. J. Shim, W. Lee, J. H. Koo, D.-H. Kim, *Adv. Mater.* **2020**, *32*, 1902743. (h) L. Wang, X. Fu, J. He, X. Shi, T. Chen, P. Chen, B. Wang, H. Peng, *Adv. Mater.* **2020**, *32*, 1901971.

[2] (a) C. Mendes-Felipe, J. Oliveira, I. Etxebarria, J. L. Vilas-Vilela, S. Lanceros-Mendez, *Adv. Mater. Technol.* **2019**, *4*, 1800618. (b) M. Xie, K. Hisano, M. Zhu, T. Toyoshi, M. Pan, S. Okada, O. Tsutsumi, S. Kawamura, C. Bowen, *Adv. Mater. Technol.* **2019**, *4*, 1800626. (c) B. Ying, Q. Wu, J. Li, X. Liu, *Mater. Horiz.* **2020**, *7*, 477. (d) P. C. Y. Chow, T. Someya, *Adv. Mater.* **2020**, *32*, 1902045. (e) W. A. D. M. Jayathilaka, K. Qi, Y. Qin, A. Chinnappan, W. S. García, C. Baskar, H. Wang, J. He, S. Cui, S. W. Thomas, S. Ramakrishna, *Adv. Mater.* **2019**, *31*, 1805921. (f) F. Narita, Z. Wang, H. Kurita, Z. Li, Y. Shi, Y. Jia, C. Soutis, *Adv. Mater.* **2021**, *33*, 2005448. (g) M. S. Irfan, T. Khan, T. Hussain, K. Liao, R. Umer, *Compos. Part A Appl. Sci. Manuf.* **2021**, *141*, 106236.

[3] (a) S. Jena, A. Gupta, *Sens. Rev.* **2021**, *41*, 320. (b) F. Niu, Z. Qin, L. Min, B. Zhao, Y. Lv, X. Fang, K. Pan, *Adv. Mater. Technol.* **2021**, *6*, 2100394. (c) Y. Zhuang, R. J. Xie, *Adv. Mater.* **2021**, *33*, 2005925. (d) T. Dinh, T. Nguyen, H. P. Phan, T. K. Nguyen, V. T. Dau, N. T. Nguyen, D. V. Dao, *Small* **2020**, *16*, 1905707. (e) T. Nguyen, T. Dinh, H. P. Phan, T. A. Pham, V. T. Dau, N. T. Nguyen, D. V. Dao, *Mater. Horiz.* **2021**, *8*, 2123. (f) L. Duan, D. R. D'Hooge, L. Cardon, *Prog. Mater. Sci.* **2020**, *114*, 100617. (g) Z. Wang, S. Guo, H. Li, B. Wang, Y. Sun, Z. Xu, X. Chen, K. Wu, X. Zhang, F. J. A. M. Xing, *Adv. Mater.* **2019**, *31*, 1805630.

[4] (a) K. Xu, Y. Lu, K. Takei, *Adv. Mater. Technol.* **2019**, *4*, 1800628. (b) W. Zou, M. Sastry, J. J. Gooding, R. Ramanathan, V. Bansal, *Adv. Mater. Technol.* **2020**, *5*, 1901036. (c) K.-J. Baeg, J. Lee, *Adv. Mater. Technol.* **2020**, *5*, 2000071. (d) J. H. Koo, J. K. Song, S. Yoo, S. H. Sunwoo, D. Son, D. H. Kim, *Adv.*

Mater. Technol. **2020**, *5*, 2000407. (e) J. Horne, L. McLoughlin, E. Bury, A. S. Koh, E. K. Wujcik, *Adv. Mater. Interfaces* **2020**, *7*, 1901851. (f) M. T. Chorsi, E. J. Curry, H. T. Chorsi, R. Das, J. Baroody, P. K. Purohit, H. Ilies, T. D. Nguyen, *Adv. Mater.* **2019**, *31*, 1802084. (g) X. Cai, B. Cui, B. Ye, W. Wang, J. Ding, G. Wang, *ACS Appl. Mater. Interfaces* **2019**, *11*, 38136. (h) C. Wang, K. Xia, H. Wang, X. Liang, Z. Yin, Y. Zhang, *Adv. Mater.* **2019**, *31*, 1801072. (i) Y. Ling, T. An, L. W. Yap, B. Zhu, S. Gong, W. Cheng, *Adv. Mater.* **2020**, *32*, 1904664. (j) Y. Gao, L. Yu, J. C. Yeo, C. T. Lim, *Adv. Mater.* **2020**, *32*, 1902133. (k) R. Yin, D. Wang, S. Zhao, Z. Lou, G. Shen, *Adv. Funct. Mater.* **2021**, *31*, 2008936.

[5] (a) S. Chen, H. Liu, S. Liu, P. Wang, S. Zeng, L. Sun, L. Liu, *ACS Appl. Mater. Interfaces* **2018**, *10*, 4305. (b) B. Yang, W. Yuan, *ACS Appl. Mater. Interfaces* **2019**, *11*, 16765. (c) O. Erol, A. Pantula, W. Liu, D. H. Gracias, *Adv. Mater. Technol.* **2019**, *4*, 1900043. (d) M. Acosta, F. Baiutti, A. Tarancón, J. L. M. M. Driscoll, *Adv. Mater. Interfaces* **2019**, *6*, 1900462. (e) S. Naficy, T. Y. L. Le, F. Oveissi, A. Lee, J. C. Hung, S. G. Wise, D. S. Winlaw, F. Dehghani, *Adv. Mater. Interfaces* **2020**, *7*, 1901770. (f) J. Cuan, Y. Zhou, T. Zhou, S. Ling, K. Rui, Z. Guo, H. Liu, X. Yu, *Adv. Mater.* **2019**, *31*, 1803533. (g) J. Song, S. Chen, L. Sun, Y. Guo, L. Zhang, S. Wang, H. Xuan, Q. Guan, Z. You, *Adv. Mater.* **2020**, *32*, 1906994. (h) J. Lee, M. W. M. Tan, K. Parida, G. Thangavel, S. A. Park, T. Park, P. S. Lee, *Adv. Mater.* **2020**, *32*, 1906679.

[6] (a) J. Lee, S. J. Ihle, G. S. Pellegrino, H. Kim, J. Yea, C.-Y. Jeon, H.-C. Son, C. Jin, D. Eberli, F. Schmid, B. L. Zambrano, A. F. Renz, C. Forró, H. Choi, K.-I. Jang, R. Küng, J. Vörös, *Nat. Electron.* **2021**, *4*, 291. (b) Y. Chen, J. Meng, Y. Xu, Y. Li, Q. Zhang, C. Hou, H. Sun, G. Wang, H. Wang, *Adv. Electron. Mater.* **2021**, *7*, 2100231. (c) M. Wang, P. Baek, A. Akbarinejad, D. Barker, J. Travas-Sejdic, *J. Mater. Chem. C* **2019**, *7*, 5534. (d) S. Choi, S. I. Han, D. Kim, T. Hyeon, D.-H. Kim, *Chem. Soc. Rev.* **2019**, *48*, 1566.

[7] (a) Y. Gao, L. Shi, S. Lu, T. Zhu, X. Da, Y. Li, H. Bu, G. Gao, S. Ding, *Chem. Mater.* **2019**, *31*, 3257. (b) Y. Gao, A. M. Nolan, P. Du, Y. Wu, C. Yang, Q. Chen, Y. Mo, S.-H. Bo, *Chem. Rev.* **2020**, *120*, 5954. (c) X.-Y. Yin, Y. Zhang, X. Cai, Q. Guo, J. Yang, Z. L. Wang, *Mater. Horiz.* **2019**, *6*, 767.

[8] (a) N. Matsuhisa, X. Chen, Z. Bao, T. Someya, *Chem. Soc. Rev.* **2019**, *48*, 2946. (b) C. Dang, M. Wang, J. Yu, Y. Chen, S. Zhou, X. Feng, D. Liu, H. Qi, *Adv. Funct. Mater.* **2019**, *29*, 1902467.

[9] (a) H. Song, Y. Sun, J. Zhu, J. Xu, C. Zhang, T. Liu, *Compos. Part B-Eng.* **2021**, *217*, 108901. (b) O. Ahmed, X. Wang, M.-V. Tran, M.-Z. Ismadi, *Compos. Part B-Eng.* **2021**, *223*, 109136. (c) T. Zhu, Q. Feng, S. Liu, C. Zhang, *Compos. Commun.* **2020**, *20*, 100376.

[10] (a) P. Shi, Y. Wang, W. W. Tjiu, C. Zhang, T. Liu, *ACS Appl. Mater. Interfaces* **2021**, *13*, 49358. (b) Y. Wang, Y. Liu, R. Plamthottam, M. Tebyetekerwa, J. Xu, J. Zhu, C. Zhang, T. Liu, *Macromolecules* **2021**, *54*, 3832.

[11] B. Ali, L. A. Qureshi, R. Kurda, *Compos. Commun.* **2020**, *22*, 100437.

[12] Y. Zheng, H. Song, S. Chen, X. Yu, J. Zhu, J. Xu, K. A. I. Zhang, C. Zhang, T. Liu, *Small* **2020**, *16*, 2004342.

[13] T. Liu, J. Peng, J. Liu, X. Hao, C. Guo, R. Ou, Z. Liu, Q. Wang, *Compos. Part B-Eng.* **2021**, *224*, 109188.

[14] (a) H. Guo, Q. Feng, K. Xu, J. Xu, J. Zhu, C. Zhang, T. Liu, *Adv. Funct. Mater.* **2019**, *29*, 1903660. (b) H. Guo, J. Zhou, Q. Li, Y. Li, W. Zong, J. Zhu, J. Xu, C. Zhang, T. Liu, *Adv. Funct. Mater.* **2020**, *30*, 2000024.

[15] Y. Xu, Q. Feng, C. Zhang, T. Liu, *Compos. Commun.* **2021**, *25*, 100693.

SUPPORTING INFORMATION

Additional supporting information may be found in the online version of the article at the publisher's website.

How to cite this article: Q. Feng, K. Wan, C. Zhang, T. Liu, *J. Polym. Sci.* **2021**, 1. https://doi.org/10.1002/pol.20210766